Relevance of infragravity waves in a wave-dominated inlet

Xavier Bertin, Maitane Olabarrieta

▶ To cite this version:

Xavier Bertin, Maitane Olabarrieta. Relevance of infragravity waves in a wave-dominated inlet. Journal of Geophysical Research. Oceans, 2016, 10.1002/2015JC011444. hal-01453412

HAL Id: hal-01453412

https://hal.science/hal-01453412v1

Submitted on 2 Feb 2017

RELEVANCE OF INFRAGRAVITY WAVES IN A WAVE-DOMINATED INLET

Xavier Bertin[1]& Maitane Olabarrieta[2]

[1]UMR 7266 LIENSs, CNRS-Universite de La Rochelle, 2 rue Olympe de Gouges, 17000 La Rochelle, France.
[2]University of Florida, Department of Civil and Coastal Engineering, Gainesville, United States.

E-mail addresses: xbertin@univ-lr.fr (Xavier Bertin); maitane.olabarrieta@essie.ufl.edu (Maitane Olabarrieta)

ABSTRACT

This study investigates the relevance of infragravity (IG) waves at Albufeira Lagoon Inlet, a shallow wave-dominated inlet located on the Western Coast of Portugal. A field experiment carried out in September 2010 revealed the occurrence of low-frequency oscillations (i.e. 25 to 300 s) in water levels and current velocities. While these fluctuations were present over the ebb-tidal delta along the whole tidal cycle, they only appeared between the beginning of the flood and up to two hours after high tide inside the lagoon. The XBeach modeling system was applied to Albufeira Lagoon Inlet and reproduced the generation and propagation of IG waves and their blocking during the ebb. This behavior was explained by blocking due to opposing tidal currents reaching 2.5 $m.s^{-1}$ in shallow water depths. Numerical results suggest that the breakpoint mechanism and the long bound wave shoaling mechanisms contributed significantly to the generation of IG waves in the inlet. IG waves induced fluctuations in flood currents inside the lagoon reaching temporarily 100 % of their magnitude. The fact that these fluctuations occur mostly at flood and not at ebb could promote flood dominance in the lagoon. This hypothesis will have to be verified, namely under storm wave conditions.

KEYWORDS

Infragravity waves, wave-dominated inlet, low frequency waves, wave blocking.

Keypoints

- Measurements revealed energetic IG waves in a wave-dominated inlet.
- Breakpoint generation and bound-wave shoaling both contributed significantly to IG wave generation.
- IG waves were blocked by opposing ebb-currents.

1. INTRODUCTION

Tidal inlets are transition zones between the ocean and back-barrier lagoons or estuaries where constant exchange of water, sediments, nutrients and larvae occurs. Hydrodynamics and morphological changes in tidal inlets have strong ecological and socio-economic repercussions, since they affect navigation safety, flooding extent, erosion of adjacent beaches, water renewal and material exchange between the lagoon (orestuary) and the open ocean. Due to the complex interactions between tides, wind waves, river outflows, sediments transport and morphology, understanding the resulting hydrodynamics and sediment transport patterns is still a challenge.

Nonetheless, an increased knowledge of these processes is needed to improve the management and maximize the resilience of these coastal systems.

In the last decade several studies (e.g. Siegle et al., 2004; Bertin et al., 2009; Olabarrieta et al., 2011; Dodet et al., 2013; Orescanin et al., 2014; Wargula et al., 2014; Olabarrieta et al., 2014, Chen et al., 2015) have emphasized the relevance of surf-zone processes in mixed-energy and wave-dominated tidal inlets. Shallow water depths over the ebb-tidal delta can induce wave breaking and subsequent surf-zone circulations. Wave-breaking accelerations can also affect the extension and direction of ebb currents, as well as impact the hydrodynamics inside the estuary. For example, wave breaking over the ebb-tidal delta can induce a wave setup and increase water levels at the scale of the whole lagoon or estuary (e.g. Malhadas et al. 2009; Bertin et al., 2009; Olabarrieta et al., 2011; Dodet et al. 2013; Arnaud and Bertin, 2014; Bertin et al., 2015). Moreover, due to the interaction between the wave bottom boundary layer and tidal currents, bottom friction increases (e.g. Grant and Madsen 1979, Soulsby et al., 1997) and,consequently, can affect the overall tidal propagation (Olabarrieta et al., 2011 and Dodet et al., 2013).

The relevance of oceanic infragravity waves (hereafter, “IG waves”) in the nearshore is well recognized and many studies have been conducted in the last four decades to ascertain their role in coastal morphodynamics (e.g. Guza et al., 1984; Masselink, 1995; Baldock and Huntley, 2002; Baldock et al., 2004; Pomeroy et al., 2012). IG waves are ocean waves with periods from 25 to more than 300 seconds associated with the presence of groups in gravity waves. To date, two main mechanisms for the generation of infragravity waves have been proposed. Longuet-Higgins and Stewart (1964) suggested that the observed free infragravity wave or “surf beat” may be due to the shoaling, release and subsequent reflection of bound long waves after the gravity waves break in the surf-zone. Bound waves result from 2nd-order non-linear wave-wave interactions between wind waves (“forced” IG waves: [Hasselmann, 1962; Longuet-Higgins and Stewart, 1962; Okihiro et al., 1996]). An alternative mechanism for the generation of surf beat was presented by Symonds et al. (1982) and Schäffer (1993), who considered the temporal variation of the breakpoint as a wave maker, generating surf beat both seaward and shoreward. The moving breakpoint mechanism can also be thought as a “dynamic set-up” in the surf-zone. Large waves break earlier and produce larger set-up than small waves in the wave group, which introduces oscillations in the set-up at the group frequency. The first mechanism was shown to be dominant on gently sloping beaches due to the shoaling of the bound-wave (e.g. List 1992; Herbers et al., 1995; Pomeroy et al., 2012) while the second mechanism occurs preferably when gravity waves break within a narrow zone, which condition is preferentially met over a steep bottom (Battjes et al, 2004; Van Dongeren et al., 2007; Baldock, 2012; Pomeroy et al., 2012).

Despite being known that mixed-energy and wave-dominated tidal inlets share characteristics of beach and tidally dominated areas (e.g. Siegle et al., 2004; Bertin et al., 2009; Olabarrieta et al., 2011), the dynamics and effects of IG waves in tidal inlets have not yet been addressed according to the author’s knowledge IG wave generation, propagation, and dissipation mechanisms in tidal inlets might differ substantially from those observed in beach environments for several reasons. First, the inlet morphology, characterized by the presence of an ebb-tidal delta, a main channel and secondary channels, is usually more complex than a beach morphology. Moreover, ebb-tidal deltas combine gentle slopes in their central part and steep slopes in their terminal lobes so that both generation mechanisms for IG waves can be active along a tidal cycle. Second, while in a beach all incoming IG wave energy is dissipated or reflected, in a tidal inlet part of the IG energy might, depending on the tidal phase, propagate through the main channel and into the inner part of the lagoon or estuary. Finally, IG waves in tidal inlets can be affected by strong flood and ebb currents.

Different types of approaches and numerical models have been considered to numerically model the generation and propagation of infragravity waves. Two main approaches or types of models can be distinguished: 1) phase-resolving (e.g, Herbers et al. 1995; Madsen et al., 1997; Kennedy et al., 2000; Torres- Freyermuth et al., 2010; Bonneton et al., 2011; Zijlema et al., 2011Ma et al., 2012; Ruju et al., 2012; Rijnsdorp et al., 2015; Sheremet et al., 2016) and 2) phase-averaged models (e.g. Reniers et al. 2004, 2006, 2010; Uchiyama and McWilliams, 2008; Long and Haller, 2009; Roelvink et al., 2009, Eldeberky et al., 2015). Phase-resolving models account for the non-linear gravity wave transformations and possible non-linear energy transfer from the IG band to the gravity band. Because of the high computational cost, the application of phase-resolving models is limited to areas of hundreds of meters and time periods shorter than a tidal cycle. On the other hand, coupled models are computationally more efficient, but they disregard the aforementioned non-linear processes.

This study is focused on the Albufeira Lagoon Inlet located on the western coast of Portugal. This wave-dominated inlet closes seasonally in autumn/early winter, usually after energetic swell conditions. Dodet (2013) simulated its morphodynamic evolution under tides and gravity waves and, although the fast morphological changes of the inlet were in overall well captured, its closure was not reproduced, as if one or several relevant processes were not accounted for in these simulations. This study tackles, for the first time, the role of infragravity waves on the hydrodynamics in a wave-dominated inlet. In particular, attention is given to the main IG wave generation mechanisms andto their interactions with tides. Possible impacts of these long waves in sediment transport and morphodynamics are also discussed.

The paper is organized as follows. A brief description of the study area is provided in Section 2. The methods, including the data acquisition and post-processing, as well as the numerical model, are described in Section 3. Observed and modeled tides, gravity and IG waves are described and compared in Section 4. Model limitations, IG wave generation and propagation mechanisms, and implications on sediment transport and morphodynamics are discussed in Section 5. The main conclusions are summarized in Section 6.

2. STUDY AREA

Albufeira Lagoon is located on the Western coast of Portugal, about 20 km South of Lisbon. The width of the continental shelf in front of the inlet is limited to 5 km due to the Lisbon Canyon (Figure 1A). The lagoon covers an elongated surface area of 1.3 km^2 SW-NE orientated and is connected to the sea through a small and shallow intermittent inlet. The inlet exhibits a strong seasonal behavior, leading to its natural closure in autumn/early winter, after which it is artificially opened in spring (Dodet et al., 2013; Fortunato et al., 2014). The inlet is bordered by steep beaches (slope of the order of 0.10) made of coarse sands (d_{50} = 0.0007-0.0018 m).

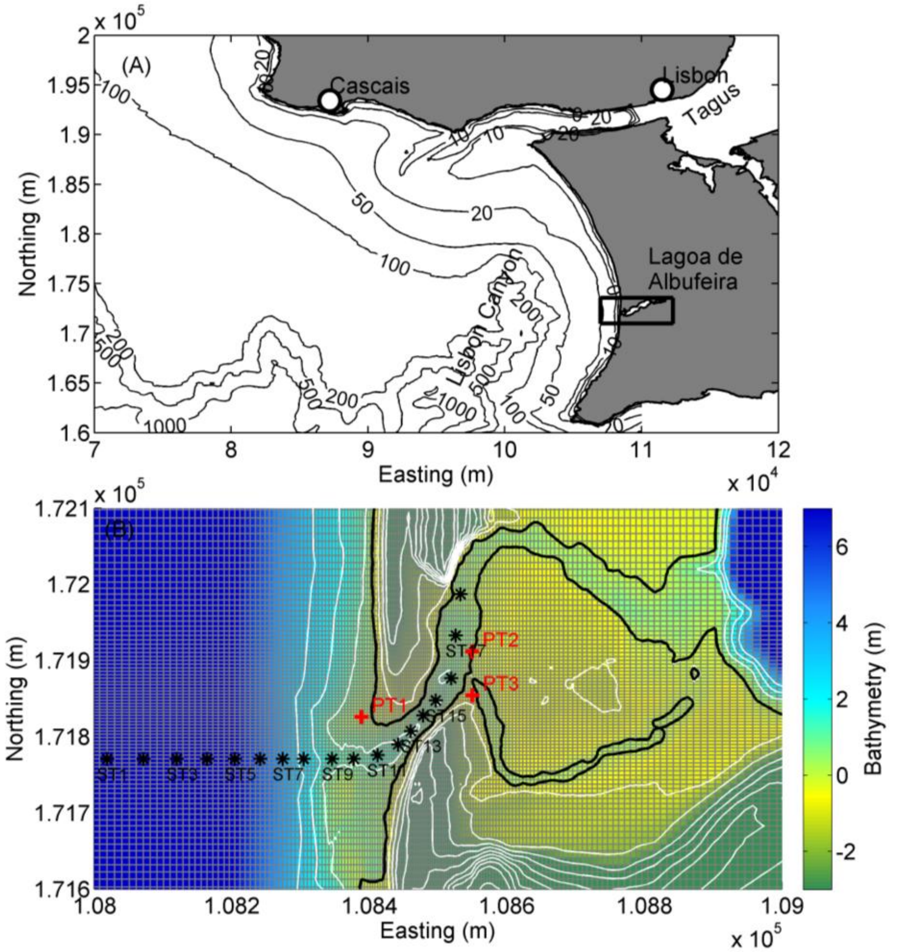

Figure1. (A) Regional bathymetry of the study area and (B) Detailed bathymetric map of Albufeira Lagoon Inlet, computational grid used for XBeach (grey frame), location of the pressure sensors (red crosses), model stations (black stars). At PT2 current velocities where also measured with an electromagnetic current-meter. The black solid line corresponds to mean sea-level contour line. The bathymetric map of the Albufeira Lagoon Inlet shown in panel B does not represent the whole computational domain. The model grid covers the whole lagoon.

This area is subjected to semi-diurnal tides, the amplitude of which ranges from less than 1 m to more than 3.5 m. The mean tidal prism during spring tides is of the order of $80 \cdot 10^4$ m^3 (based on the numerical estimates of Fortunato et al., 2014). Tides are strongly distorted throughout their propagation across the inlet, semi-diurnal tidal constituents are severely damped while quarter-diurnal and fortnightly non-linear constituents develop. Inside the lagoon, the amplitude of the semi-diurnal constituents experiences a seasonal cycle, with a maximum in late summer after which it decreases until the lagoon closes. This behavior is commonly observed at other Portuguese shallow inlets and was explained by the shoaling of the inlet due to several wave-induced processes (Bertin et al., 2009; Dodet et al., 2013).

The study area is exposed to an energetic wave climate, particularly in winter. Based on a 57-year wave numerical hindcast (Dodet et al., 2010), the mean annual deep water (10.0ºW; 38.0ºN; ~ 3000 m deep) significant wave height (H_{m0}), mean direction (MWD) and peak period (T_p) are respectively 1.9 m, 312 °, and 10.5 s. During winter (resp. summer) the corresponding values are: 2.5 m, 305 °, and 12.1 s (resp. 1.3 m, 319° and 8.4 s). The drainage basin of the Albufeira Lagoon covers a surface area of around 106 km^2, but the freshwater discharge is only significant under heavy rain, which usually occurs when the lagoon is closed.

3. METHODS

IG wave dynamics and their relevance in Albufeira Lagoon are analyzed combining field measurement analysis and numerical modelling. Water levels and currents were measured in the field experiment described by Dodet et al. (2013). The experiment was not specifically designed to study IG waves, and, therefore, the location of the instruments prevents the understanding of the main generation and propagation mechanisms from the data analysis. To complement the analysis and ascertain the main IG wave generation and propagation mechanisms, we applied the modeling system XBeach (Roelvink et al., 2009), version 1.21.3866M, 'Groundhog Day' release.

3.1 Field measurements

During the Albufeira Lagoon Inlet field experiment, water levels and currents were measured on the ebb-tidal delta (PT1), on the flood-tidal delta (PT2) and at the tip of the sand-spit (PT3) located on the southern margin (Figure 1B). A high-resolution Acoustic Doppler Current Profiler (ADCP) was collocated at PT1, while and electromagnetic current-meter was collocated at PT2. Pressure measurements were first corrected from the atmospheric pressure variations. The entire record was split into consecutive bursts of 30 minutes and the bursts in which the sensor was alternatively dry were not considered. Bottom pressure energy density spectra *Ep(f)* were computed using Fast Fourier Transform, with 2 Hanning-windowed segments (32 degrees of freedom). Considering that the spectral integrals are Chi-square distributed, confidence intervals (hereafter CI) for a given level α were computed according to Bendat and Piersol (1971):

$$CI = \left[\frac{\nu}{\chi^2_{\nu,1-\alpha/2}} ; \frac{\nu}{\chi^2_{\nu,\alpha/2}} \right]$$

These pressure spectra were then converted into elevation spectra *E(f)* considering the linear wave theory. The significant wave height (H_{m0}) was computed as:

$$H_{m0} = 4\sqrt{m_0} \qquad (1)$$

Where,

$$m_0 = \int_{f_{\min}}^{f_{\max}} E(f)\,\partial f \quad (2)$$

Where f_{min} and f_{max} were set to 0.04 and 0.5 Hz for the gravity band and 0.002 and 0.04 *Hz* for the infragravity band, respectively.

3.2 Numerical model

XBeach is a two-dimensional modelling system that couples the St. Venant equations with a simplified wave-action conservation model, a sediment transport and bed update model. To simulate the generation and propagation of IG waves, XBeach can be forced with time varying directional wave spectra defined at the boundaries. Since the wave spectra do not contain the phase information, the model assumes random phases and applies a single summation technique to reconstruct the free surface elevation time series at the boundaries. A Hilbert transform is applied to derive time series of the gravity wave energy (that varies at the wave group scale) and these are imposed as boundary conditions for the wave-action balance equation. The incoming bound-wave is computed following Herbers et al. (1994), and is imposed along the open boundary of the flow model.

In this study, depth-induced wave breaking energy dissipation was computed using the parameterization proposed by Daly et al. (2012). Wave-current interactions are also considered in the model. The interaction between currents and gravity waves is included in the gravity wave dispersion relation modified by the Doppler Effect and in the eikonal equation. Dissipation of gravity waves by whitecapping induced by opposing current is not considered. The dynamics of IG waves, including their generation and propagation, are implicitly considered by the St. Venant equations. Therefore, the effects of currents on IG wave propagation, including their possible blocking, are represented by the equations and do not need to be explicitly included. The reader is referred to Roelvink et al. (2009) for a detailed description of XBeach.

A rectilinear grid (with variable grid size) covering the whole lagoon and extending to offshore water depths of 20 m was implemented. The spatial resolution ranged from 20 m along the open boundary to 3 m at the inlet (Fig. 1B). Such a fine resolution was required to adequately represent the inlet channel and resulted in a 210 by 380 nodes grid. Along the open boundaries, XBeach was forced with time-series of water levels recorded at the nearby Cascais tide gauge (Fig 1A) and the time varying directional wave-spectra originated from an application of SWAN (Booij et al., 1999) at the scale of the Cascais Bay as described in Dodet et al. (2013). This SWAN run was forced along its open boundaries with time series of wave energy spectra computed from an application of the WaveWatchIII model (Tolman, 2009) at the scale of the Atlantic Ocean (Crawford et al., 2015) and forced with wind fields originating from the ERA-INTERIM reanalysis (Dee et al., 2011).

Bottom friction was represented by a non-linear quadratic bottom shear stress with a constant Chezy coefficient (equal to 30 $m^{0.5}.s^{-1}$). The horizontal eddy viscosity was assumed constant (0.5 m^2/s). The minimum water depth was set to 0.2 m and 0.25 m for the computation of the Stokes velocities. The breaking parameter γ was set to 0.4 and γ_2 to 0.3. These values provided the best agreement between measured and modeled free-surface elevations and velocity magnitudes.

The model was run for the duration of the field experiment (2 days), and time series of surface elevation, current velocities were archived at a 5 s interval. Spectral estimates were computed following the same methodology as for the field observations (section 3.1). To analyze the IG wave generation mechanisms and their relevance different simulations were run (Table1). In all of them tidal propagation was taken into account. Run 0 did not consider gravity waves, only tides. Run 1, considered tides and gravity waves but wave groups were not taken into account.

Run 2 included the effect of tides, gravity waves and wave groups. Run 3 is the same configuration as Run 2 (considers the same random phases to reconstruct the wave envelope signal) but wave forces were turned off when the gravity waves were breaking. In Run 4, wave forces were turned off outside the surf-zone and the incoming bound wave at the boundaries were turned off, so that only the wave breaking variation at the scale of the wave groups contributes to the IG wave generation. Run 5 did not include any wave forces and it only propagated the tide and the incoming bound wave defined at the boundaries. Runs 3 to 5 were designed to analyze the relative contribution of the different IG wave generation mechanisms. To ensure that runs 1 to 5 had the same model setting, we first ran Run2 and we stored the wave-group changing energy and flux boundary conditions. These were directly used in runs 3 to 5. Since Run1 did not account for the gravity energy modulation, the previously stored energy boundary condition was low-pass filtered and imposed in Run 1. For model/measurement comparison shown in section 4, 7 more simulations (Run 6 to 12) were done considering tides, gravity and IG waves (same configuration as run 2). The ensemble-mean of these realizations was used for the model verification.

	Run0	Run1	Run2	Run3	Run4	Run5	Runs 6-12
Tides	Yes	Yes	Yes	Yes	Yes	Yes	Yes
Gravity waves	No	Yes	Yes	Yes	Yes	No	Yes
IG waves	No	No	Yes	Yes	Yes	No	Yes
Radiation stress inside surf-zone	No	Yes	Yes	No	Yes	No	Yes
Radiation stress outside surf-zone	No	Yes	Yes	Yes	No	No	Yes
Bound wave at offshore boundary	No	No	Yes	Yes	No	Yes	Yes

Table 1. Characteristics of the numerical simulations.

4. RESULTS

Tidal and gravity wave characteristics during the field experiment are described by Dodet et al. (2013) and will not be the main focus of this section. However, since gravity waves and IG wave propagation and generation can be affected by water levels and tidal currents model results are going to be dependent on how well water levels and currents are reproduced by the model. Therefore, it is necessary to verify modeled water levels and currents and to show the comparison between modeled and measured tidal and gravity waves for a correct interpretation of the results.

4.1 *Tidal propagation across the inlet*

The field experiment covered 3 tidal cycles and took place during spring tide conditions (Figure 2). The mean tidal range was 2.45 m, with a minimum of 2.31 m and a maximum of 2.54 m. The tidal wave offshore the Albufeira Lagoon is symmetric, but the non-linear tidal propagation through the inlet produces significant distortion (see Figure 3.a). As a consequence, the tidal range inside the lagoon was reduced by more than 50% compared to the ocean. As usually observed in friction-dominated tidal inlets, the mean water level inside the lagoon increased compared to the ocean, although mean water levels inside the lagoon were also affected by wave induced forces (Dodet et al., 2013). In overall, tidal propagation was well reproduced with the numerical model as reflected in the model skill values (see Table 2).

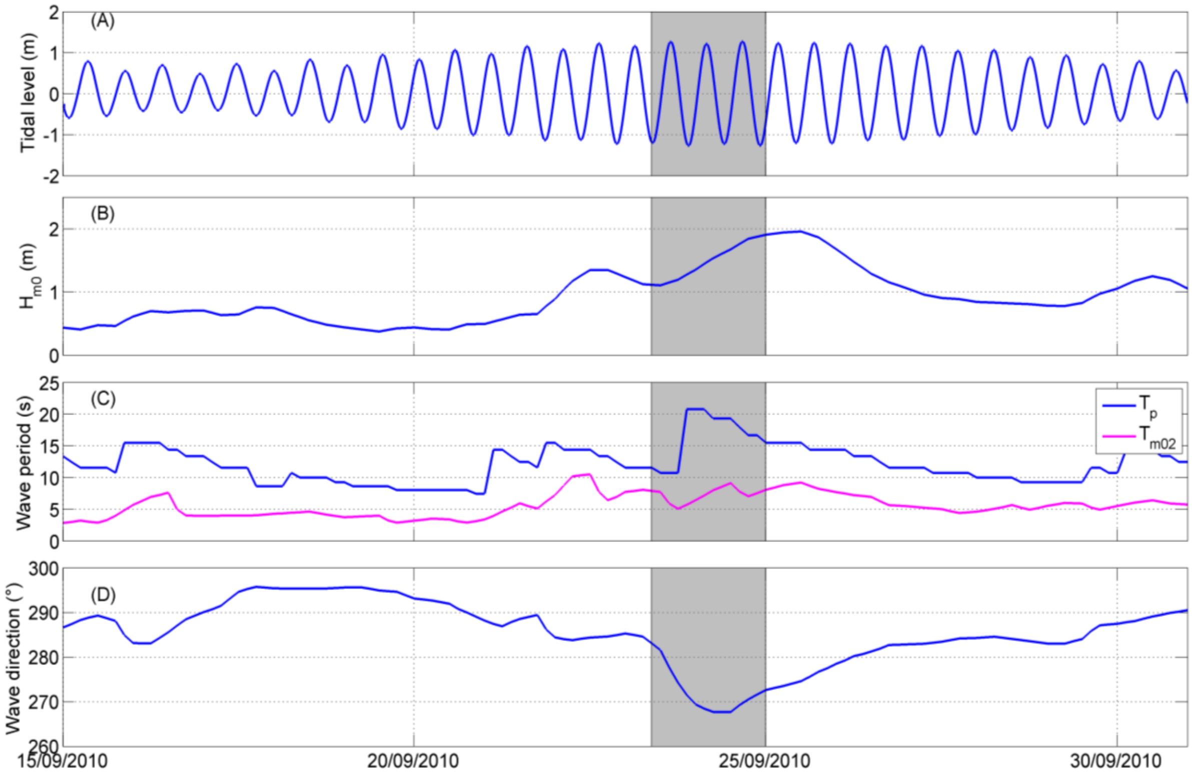

Figure 2. Offshore hydrodynamic conditions during the 15th and 31st of September 2010, (A) tidal level measured at the tidal gauge nearby Cascais, (B) deep water significant wave height, (C) deep water wave periods, and (D) deep water mean wave direction. Deep water wind wave characteristics were computed with Swan model, offshore the inlet at a water depth of 100 m. The shadowed area represents the period of the field experiment.

The Root Mean Square Error (RMSE) between modeled and measured water level variations at the ebb-tidal delta station (PT1) was 0.07 m, at PT12 0.08 m and 0.06 m at PT3. These values were still smaller than 10% of the tidal range at each station, which indicates that the model reproduced adequately the tidal distortion as its propagation through the inlet and inner lagoon.

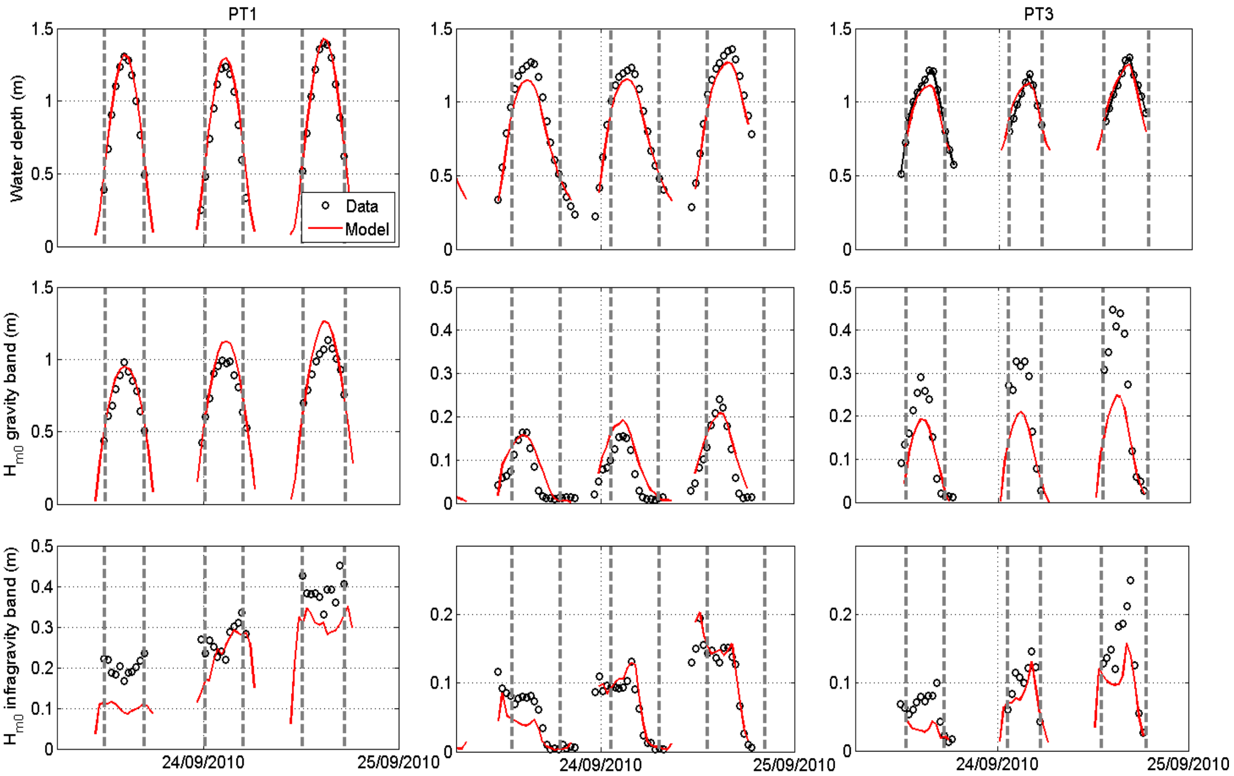

Figure 3. Measurement (black circles) and model result for Run2 (red curve) comparison at the three measurement stations. Top panels show the low-pass filtered (*f*<0.002 Hz) free surface elevation time series, middle panels $H_{m0,G}$ time series and bottom panels $H_{m0,IG}$ time series. The grey dashed vertical lines indicate a similar water level at ebb and flood and help identifying large differences in short and IG waves between ebb and flood. Model results represent the ensemble-mean of 8numerical simulations, statistically equivalent to Run2.

Currents were also measured at PT2 by means of an electromagnetic current meter, located 0.4 m above the bed. The comparison with modeled currents averaged over 30 minute samples at this sensor reveals a fair agreement, with a RMSE of 0.10 m/s and only a slight underestimation of the flood peak, leading to a -0.05 m/s negative bias (Figure 4) and a 0.98 Willmott Skill Score (WSS) (Table 3). However, since this sensor was located on the ramp of the flood-delta (Figure 1), it was sheltered from ebb currents. In the main channel (ST 13) modeled ebb currents were twice as strong as flood currents and temporarily reached 2.5 m/s (Figure 4).

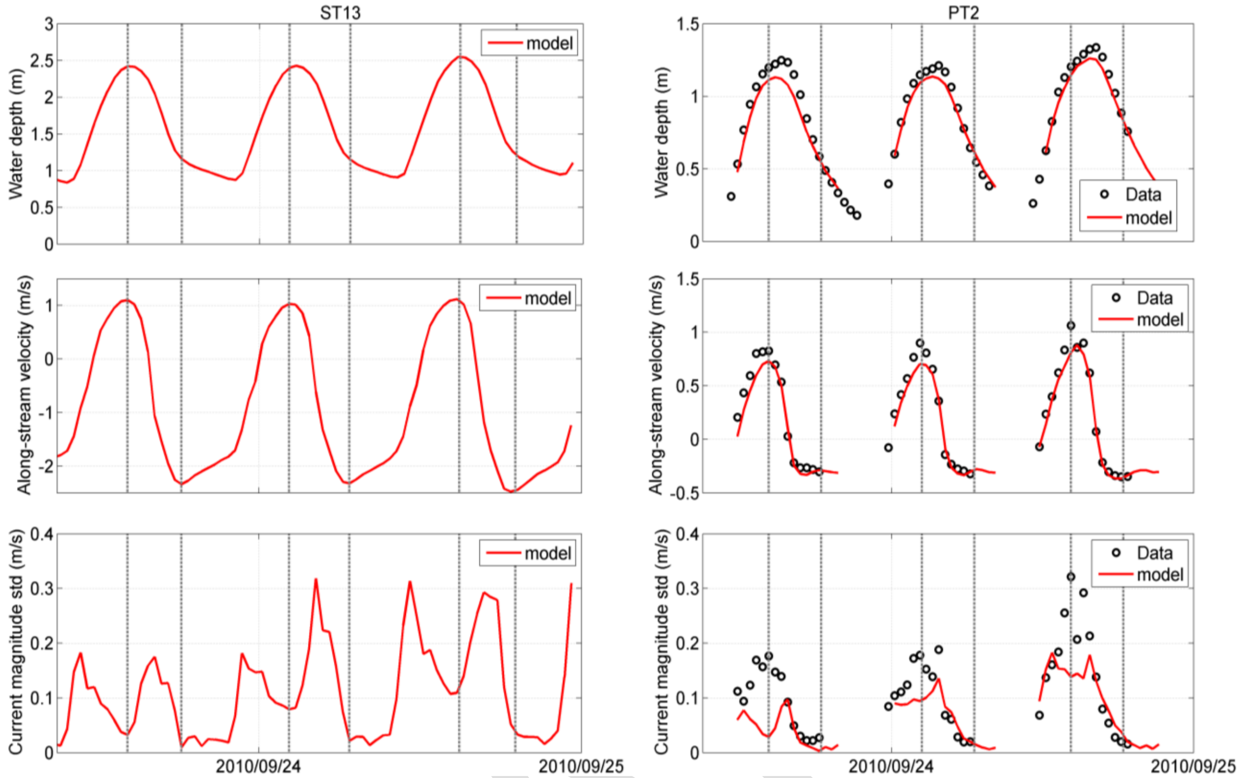

Figure 4. Modeled (red) against measured (black circles) water depth (top row), along-stream current velocity (middle row) and standard deviation of the current magnitude computed over 30 minute samples (bottom row) in the inlet main channel (ST13, Figure 1) and at PT2. The grey dashed lines indicate the time where maximum flood and ebb currents occurred. The standard deviation of the current magnitude computed over 30 minute samples has been previously low-pass filtered with a 25 s window to remove orbital motions of gravity waves.

4.2 Characterization of gravity waves

Deep-water gravity wave energy and the peak period (T_p) increased during the field experiment (Fig2). The 23rd of September T_p was 12.5 s and the significant wave height ($H_{m0,G}$) 1 m. At the end of the experiment swell waves propagating from the west hit the inlet, and consequently T_p and $H_{m0,G}$ increased to more than 20 s and 1.8 m respectively.

In all the stations, gravity waves were depth limited and, therefore, tidally modulated (Figure 3). Maximum $H_{m0,G}$ were observed during high tide at PT1, especially in the last tidal cycle, when values over 1.2 m were measured. This station became dry from mid to low tide. At PT1 the model RMSE was 0.09 m (see Table 2), and the tidal modulation was well captured. The Willmott Skill Score (defined in Appendix A) was larger than 0.92 at PT1 and PT2, and decreased to 0.76 at PT3, mostly due to a negative bias.

Gravity waves damped when propagating from the ebb-delta to the inner lagoon (Figure 3). $H_{m0,G}$ decreased from PT1 on average ~91% at PT2 and ~76% at PT3 during high tide. Modeled

$H_{m0,G}$ mean reductions were ~86% at PT2 and ~84% at PT3. The highest RMSE (~0.10 m) was obtained at PT3, where the model underestimated $H_{m0,G}$, especially during the last high tide.

During the ebb, $H_{m0,G}$ at PT2 decreased sharply and at mid-ebb $H_{m0,G}$ was lower than 0.025 m (Figure 3). This fast reduction after the beginning of the ebb up to low tide was already explained by wave blocking at the inlet (Dodet et al., 2013). The $H_{m0,G}$ tidal modulation observed in the measurements was well reproduced with the numerical model. However, the blocking during the mid-ebb was underestimated by the model.

4.3 Characterization of IG waves

Measurements revealed the occurrence of low frequency oscillations (i.e. 25 to 300 s) in the ebb-delta (PT1) and interior stations (PT2 and PT3). During the experiment, IG wave significant wave height ($H_{m0,IG}$) increased from 0.2 m to more than 0.5 m at the ebb-tidal delta (PT1). The largest $H_{m0,IG}$ was observed during the last tidal cycle of the 24th of September, when offshore wind waves where most energetic and the period was largest (see Figure 2). This swell originated from a remote storm (Dodet et al., 2013).

Mirroring the behavior of the gravity band, IG waves were tidally modulated and $H_{m0,IG}$ decreased from the ebb-tidal delta (PT1) to the inner part of the lagoon (Figure 3). Due to the shallow water levels at PT1, the station became dry during half of the tidal cycle. In the three tidal cycles covered by the experiments, two local maxima of $H_{m0,IG}$ could be identified at PT1, the first before and the second after high tide. Between these two local maxima, specifically during high tide, a local minimum of $H_{m0,IG}$ was observed.

At PT2 and PT3, the observed tidal modulation was not related to the drying of the stations, since they only became dry at the lowest tidal levels. After mid-ebb, IG wave energy levels at the inner stations were very low ($H_{m0,IG}$ decreased by more than 90% with respect to the maximum values observed during each tidal cycle), suggesting a possible blocking of IG waves. As an example, Figure 6 depicts the water elevation measurements at PT2. The water elevation time series, showed fluctuations both in the gravity and IG bands, especially during late flood, high tide and at the begin of the ebb. After high tide, as the water elevation decreased, $H_{m0,G}$ and $H_{m0,IG}$ decreased drastically. $H_{mo,G}$ reduction occurred on average 20-25 minutes before the decrease of the IG band.

XBeach captured both the IG wave energy decrease from the ebb-tidal delta to the inner part of the lagoon and the tidal modulation (see Table 2). At PT1 the model tended to underestimate the observed IG wave energy levels, particularly during the first tidal cycle (RMSE=0.08 m), while at PT2 and PT3 $H_{m0,IG,}$ model results were closer to the measurements (RMSE=0.02 and 0.04 m at PT2 and PT3 respectively). As indicated by the Willmott Skill Score the model performance was good in all the stations. As observed in the measurements, model results showed an increase of the $H_{m0,IG}$ just before and after the high tide, with a local minimum at high tide. Although this tendency was observed in all the stations, it was more pronounced at PT3, especially during the last tidal cycle. As observed in the measurements, modeled IG waves almost disappeared after mid-ebb at PT2 and PT3.

In addition to bulk parameters, measured and modeled frequency distributions of the energy associated with IG waves were also compared during the flood (T1) and during the ebb periods of the second tidal cycle (Figure 5). At PT1, the frequency distribution of the IG wave energy was well captured by the model, although the energy level of the gravity band was underestimated by the model. In particular, the maximum of energy was found in the same frequency band in the model and in the measurements (0.02-0.04 Hz). The wave spectrum during flood and ebb did not change significantly. Inside the lagoon (PT2 and PT3), the frequency repartition of energy was also well captured by the model during the flood, particularly at PT2, which mirrors the good agreement between model and data for $H_{m0,IG}$ (Figure 3). During the ebb, the two orders of magnitude drop of energy at the highest frequencies was well captured by the model, particularly at PT2.

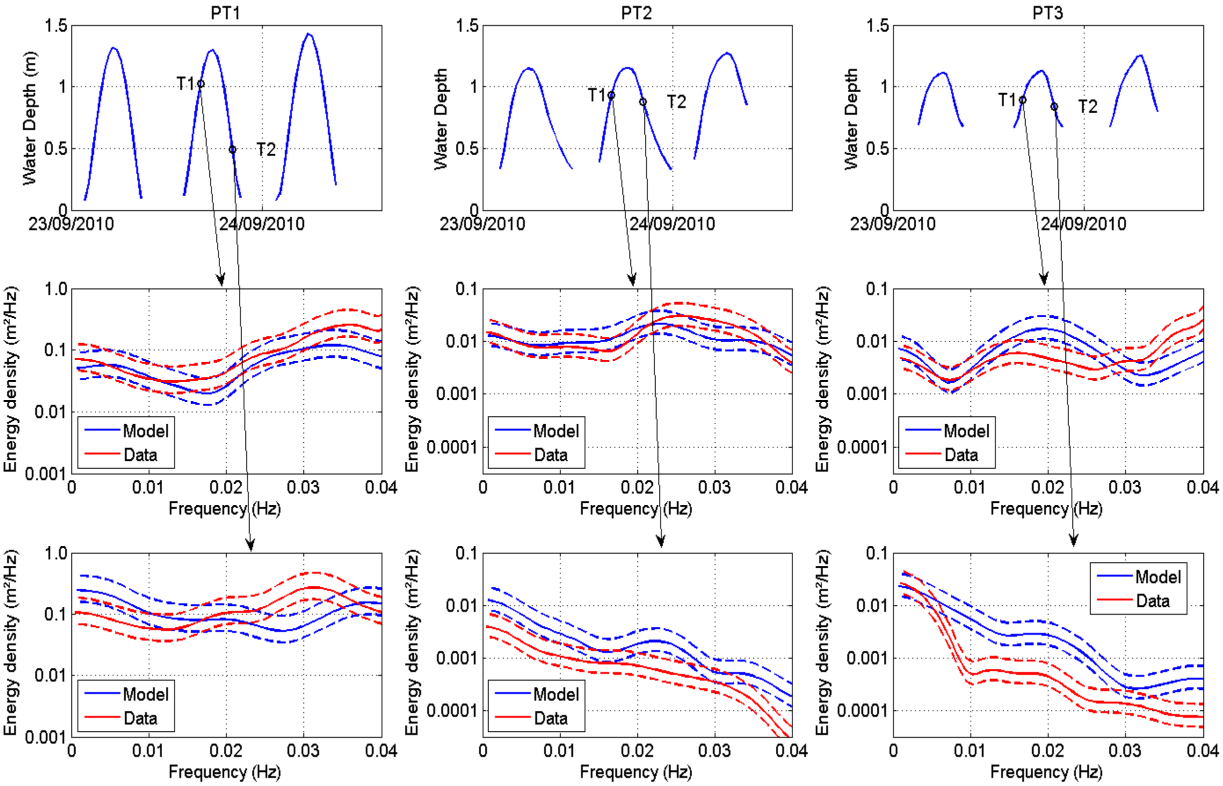

Figure 5. Water depth (top row), IG wave energy density spectra of energy at T1 (middle row) and IG wave energy density spectra of energy at T2 (bottom row) at PT1 (left column), PT2 (middle column) and PT3 (right column). Measured and modeled spectra are depicted in red and blue respectively. Dotted lines represent the 95% confidence interval of the spectra.

Low frequency fluctuations in the range 25 to 300 s were also observed in the currents velocities recorded at PT2 (Figure 4). The largest current fluctuations in the infragravity band occurred nearly in phase with maximum flood currents and rapidly dropped after the beginning of the ebb. After mid-ebb, these current fluctuations were almost inexistent. XBeach captured reasonably the time evolution of these velocity fluctuations, although with a substantial underestimation of the peak (Figure 4).

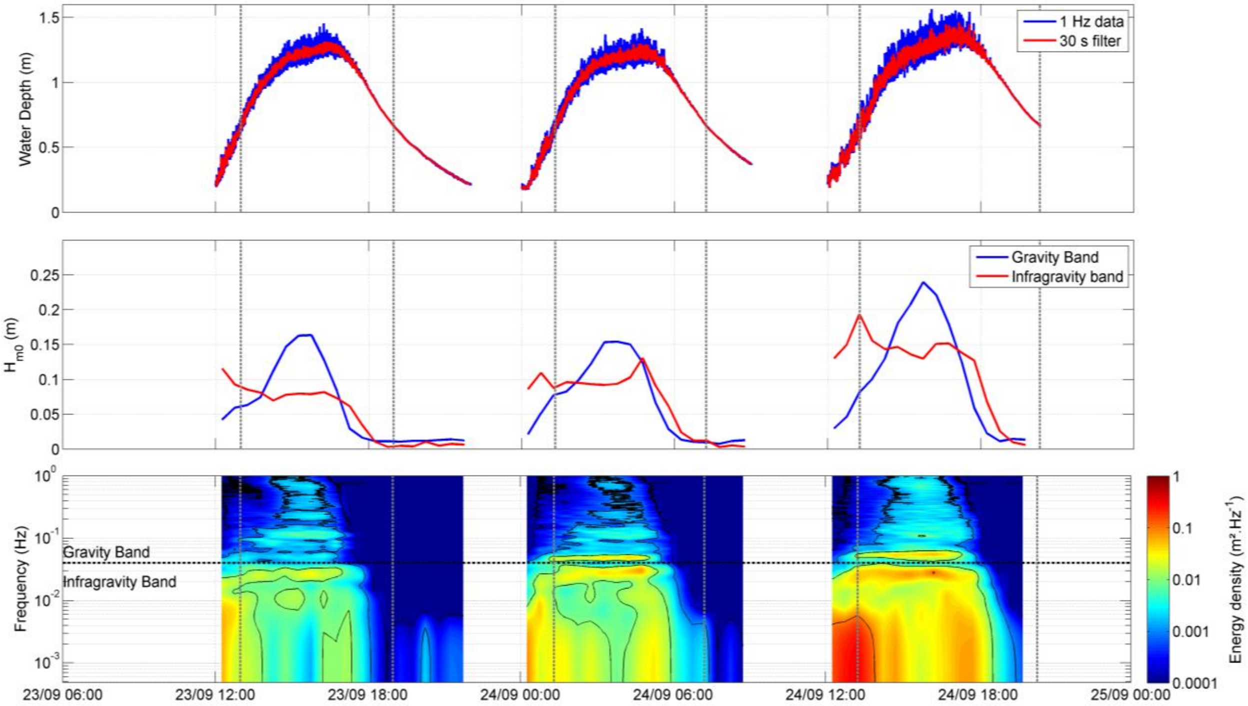

Figure 6. Time series of the measured free surface elevation (top), $H_{m0,G}$ and $H_{m0,IG}$ (middle), and frequency repartition of energy density (bottom) at PT2.

	Free surface elevation (tides+ wave setup)				$H_{m0,G}$					$H_{m0,IG}$		
	RMSE (m)	NRMSE (%)	BIAS (m)	WSS	RMSE (m)	NRMSE(%)	BIAS (m)	WSS	RMSE (m)	NRMSE (%)	BIAS (m)	WSS
PT1	0.07	6.7	0.06	0.98	0.09	11	0.07	0.95	0.08	28	-0.07	0.79
PT2	0.08	8.5	-0.06	0.98	0.03	44	0.02	0.92	0.02	24	-0.004	0.96
PT3	0.06	6	-0.03	0.94	0.1	48	-0.07	0.76	0.04	41	-0.03	0.805

Table 2 Root Mean Square Error (RMSE), Normalized Root Mean Square Error (NRMSE), bias and model skill (Willmott Skill Score, WSS) for free surface elevation (tides+ wave setup), $H_{m0,G}$and $H_{m0,IG}$. For a perfect model that reproduces the observation exactly, the WSS is one.

	RMSE (m/s)	Bias (m/s)	NRMSE (%)	WSS (-)
Along-stream current magnitude	0.10	-0.05	21	0.98
Current magnitude standard deviation	0.07	-0.04	53	0.76

Table 3 Root Mean Square Error (RMSE), bias, Normalized RMSE and model skill (Willmott Skill Score, WSS) for current magnitude and standard deviation.

5. DISCUSSION

This section points out the limitations of the considered modeling approach, and describes the main mechanisms that trigger IG waves in Albufeira Lagoon and the propagation processes along the tidal inlet. In the absence of water level measurements outside the surf-zone, it was not possible to analyze the dominant IG wave generation mechanism based on the observations. Considering that XBeach reproduced IG energy evolution reasonably both inside and outside the lagoon, we used model results alternatively. The section also discusses the possible implications of IG waves on sediment transport and morphodynamics in wave-dominated inlets.

5.1 Limitations of the modeling approach

The comparison between modeled and measured water levels showed a good agreement, with RMSE lower than 0.1 m. Wave heights in the gravity band ($H_{m0,G}$) were also reasonably reproduced, with RMSE ranging from 0.04 to 0.10 m. On the ebb-tidal delta $H_{m0,G}$ were slightly overestimated at high tide. This problem was also pointed out by Dodet et al. (2013) and explained by limitations in the available bathymetric data. Inside the lagoon, the model overestimated wave heights at the beginning of the ebb, although the total blocking that occurred after mid-ebb was well captured. The fast drop of wave height at the beginning of the ebb was explained by Dodet et al. (2013) by an increase in wave steepness due to strong opposing currents, which induces dissipation by whitecapping. The increase in wave steepness is due to shoaling induced by opposing currents. This hypothesis was corroborated by time series of wave energy spectra (Figure 6), which shows that the highest frequencies were dissipated first. Since XBeach considers a single frequency in the gravity band, this process cannot be accurately represented, and could explain the overestimation of wave height at the beginning of the ebb. The under prediction of $H_{m0,G}$ at PT3 and over prediction at PT2 during the flood and high tide could also be due to the fact that we are not considering any diffraction effects.

$H_{m0,IG}$ time series were reasonably reproduced, with RMSE of the order 0.02 to 0.08 m. In particular,$H_{m0,IG}$ were underestimated by up to 25%, and even 50% at the first tidal cycle at PT1(Figure 3). Among the different possible reasons, the fact that IG and gravity waves are represented in different models doesn’t allow a proper representation of all the non-linear interactions that can affect the generation, propagation and dissipation of IG waves. For instance, the merging of bores in the surf-zone (e.g. Senechal et al., 2001; van Dongeren et al., 2007) cannot be represented in such modeling approach, which would lead to an overestimation of energy in the gravity band and an underestimation in the IG band, as observed here. These model limitations, together with the limitations in the available bathymetric data could explain why at PT1 the WSS indicates a lower model performance. This underestimation of IG waves can also explain the underestimation of low frequency fluctuations in the currents observed at PT2 (Figure 4). In addition, the relationship between $H_{m0,IG}$ at the entrance of the lagoon and the magnitude of the current fluctuation inside the lagoon doesn’t appear to be linear. This non-linearity could be related with the rapidly changing bathymetry around the flood delta but this hypothesis will have to be verified in future studies.

However, despite these limitations, the low RMSE and acceptable model skills values would suggest that XBeach captures the main processes responsible for IG wave generation and propagation during the experiment. Therefore, the following points of the discussion rely on numeric results and experiments, intended to better understand the relevance of IG waves on tidal inlet dynamics.

5.2 IG wave generation

With the free surface elevation stored at each computational node with a 5 s interval, for each model simulation, the time variation of the IG energy variance was computed every 10 minutes. The energy variance evolution, through a transect that extended from offshore of the inlet (at water depths of 10 m), along the main channel, to the interior part of the lagoon, was analyzed and compared between the considered simulations (Figure 7). Model stations (hereafter ST) chosen for the data analysis are shown in Figure 1.

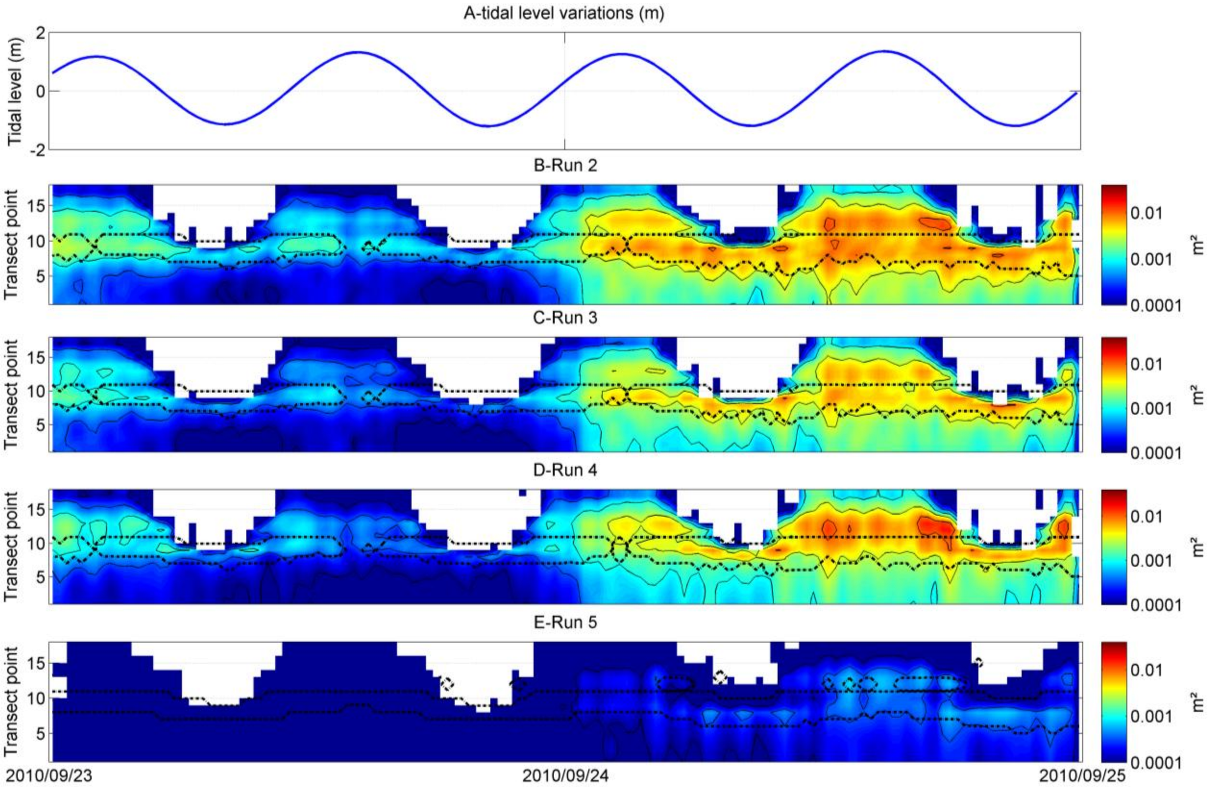

Figure 7.A) Time series of the tidal free surface elevation at ST2, and time series of the simulated *IG wave* energy along the transect shown in Figure 1: B) Run2: with incoming bound wave and wave forces activated everywhere, C) Run3: same as 2 without wave forces in the surf-zone, D) Run4: no incoming bound-wave nor wave forces outside the surf-zone, E) Run5: with incoming bound-wave and without wave groups. The locations of stations along the selected transect are shown in Figure 1. The dashed lines delimit the surf-zone.

In general, energy levels at Run 2 and 4 were higher than at 3 and 5. In Run 2 the maximum energy levels where 0.012 m^2, which is equivalent to $H_{m0,IG}$ of 0.45 m. In all simulations energy increased from offshore to the ebb-tidal delta (ST 7-11), where maximum values were reached. When water levels exceeded mean water levels two local maxima were observed. The first one was located in the offshore edge of the ebb-tidal delta, between ST 8 and 10. The second was located in the inlet mouth, between ST 12 and 14. During the rest of the tidal cycle only one maximum, at the edge of the ebb-tidal delta, was observed. The location was tidally modulated, closer to the inlet at high tide and more offshore at low tide. Energy was higher inside the surf-zone for run 4 and conversely, slightly higher outside the surf-zone for Run 3. Run 5 was designed to investigate the contribution of the incoming bound wave and its shoaling across the domain without any further forcing mechanism (Figure 7E). The IG energy variance in Run 5 was one order of magnitude smaller than in the rest of the runs, which indicates that this mechanism is not dominant, therefore it will not be further discussed.

Run 3 was designed to compute the contribution of the bound wave mechanism in IG wave generation while Run 4 was designed to isolate the contribution of the breakpoint mechanism. In order to better quantify the contribution of each mechanism, we also computed the ratio between IG energy variance from Run 3 (resp. Run 4) normalized by the linear sum of the IG energy variance from Run 3 and 4 (Figure 8B and 8C, respectively). Outside the surf-zone and up to the middle of the surf-zone, the bound wave mechanism is responsible for 40 to 70 % of the IG energy variance, while from the inner part of the surf-zone to the shoreline and the inlet mouth, the breakpoint mechanism turns dominant at the lower stages of the tide and is responsible for 50 to 90% of the IG energy variance. During high-tide, the relevance of the breakpoint mechanism decreases, which could be due to less intense wave breaking over the steepest part of the ebb-shoal. This behavior would also explain the shapes of the observed time series of $H_{mo,IG}$ measurements, with two local maxima (one at flood and the other at ebb tide) and a local minimum during high-tide.

In order to detect possible interactions between both mechanisms, we computed the linear sum of the IG energy variance from Run 3 and 4 normalized by the IG energy variance of Run 2 (Figure 8D). All along the considered time series, the normalized sum is close or higher than 100%, with local values reaching 200% along the shoreline. This behavior suggests that the bound-wave and the breakpoint mechanisms acted in opposite ways and resulted on a reduction of $H_{m0,IG}$ compared to a situation where both mechanisms would act independently. Since the bound-wave is out of phase with the wave envelope and the wave setup is in phase, the combination could create a destructive interaction and result on a reduction of the amplitude of the observed IG waves. In addition, Run 3 does not include wave forces inside the surf-zone and therefore the mean wave setup is not accounted for. Additional tests with a simple 1D shoaling model (energy flux conservation) suggest that considering wave setup could reduce IG wave energy by ~8 %. Therefore, this effect could also contribute to explain departures from 100 % in Figure 8D.

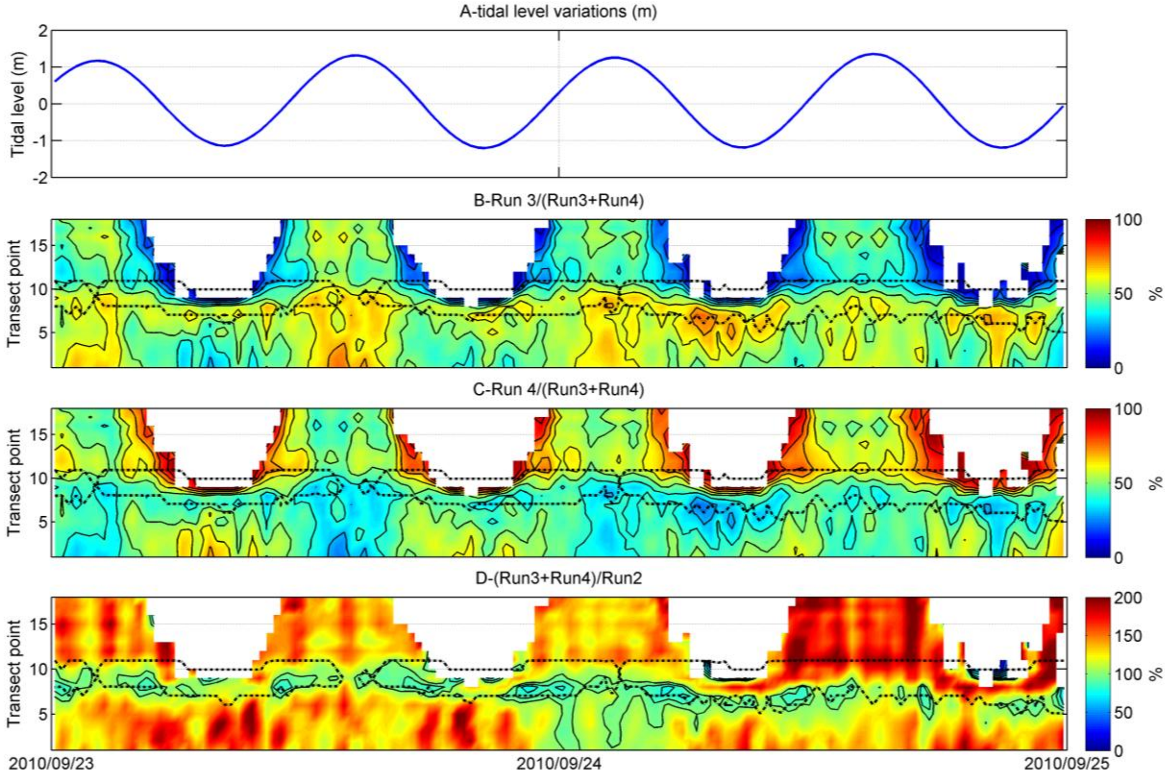

Figure8. A) Time series of the free-surface elevation due to tides in ST2. (B) Percentage of *IG energy variance* due to bound wave mechanism compared to breakpoint mechanism, C) Percentage of *energy variance* due to breakpoint mechanism compared to bound wave mechanism and D) Sum of energy variance of Run 3 and Run 4 normalized by Run 2, showing relevant interactions between both mechanisms.

5.3 IG wave propagation from the ebb-tidal delta to the inner lagoon

IG wave propagation from the ebb-tidal delta to the inner part of the lagoon is complex and highly dependent on the tidal phase. $H_{m0,IG}$ variation from the offshore to the inner part of the lagoon showed that, independently of the tidal phase, the maximum IG energy peak was obtained over the ebb-tidal delta (Figure7). This maximum was followed by a decrease of $H_{m0,IG}$ between ST 10 and 12. At the inlet throat (ST 13 and 14) a second local minimum was observed during the flood and high tide. During low and ebb tide a drastic decrease of $H_{m0,IG}$ was detected at ST 13, in the modeling results as in the observations.

To have a better understanding of how the tidal stage can affect the IG wave propagation, we computed the spatial distribution of $H_{m0,IG}$ at different tidal instants during the last tidal cycle (Figure 9), assuming stationary mean wave boundary conditions equivalent to those of September 24 at 9:00 AM ($H_{m0,G}$=1.55 m, T_p= 19.3 s and 264 degrees peak direction in nautical convention). $H_{mo,IG}$ was computed after splitting the modeled free-surface elevation into consecutive bursts of 30 minutes. To be consistent with this burst, currents were also averaged over 30 minute intervals.

Model results indicate that during maximum ebb and low tide, the maximum $H_{m0,IG}$ was restricted to the terminal lobe, whereas during high tide and mid flood infragravity energy propagated throughout the ebb-tidal delta. During mid ebb, IG wave energy reached the inlet mouth but the energy did not propagate into the lagoon, it got blocked. Tidal currents at the inlet were more intense than 1.8 m/s, reaching peak values of 2.5 m/s in water depths ranging from 1 to 1.5 m (Figure 4). As the water depth decreased parts of the ebb-tidal delta became dry. IG waves were mainly generated in the terminal lobe, where most of the wave breaking occurred.

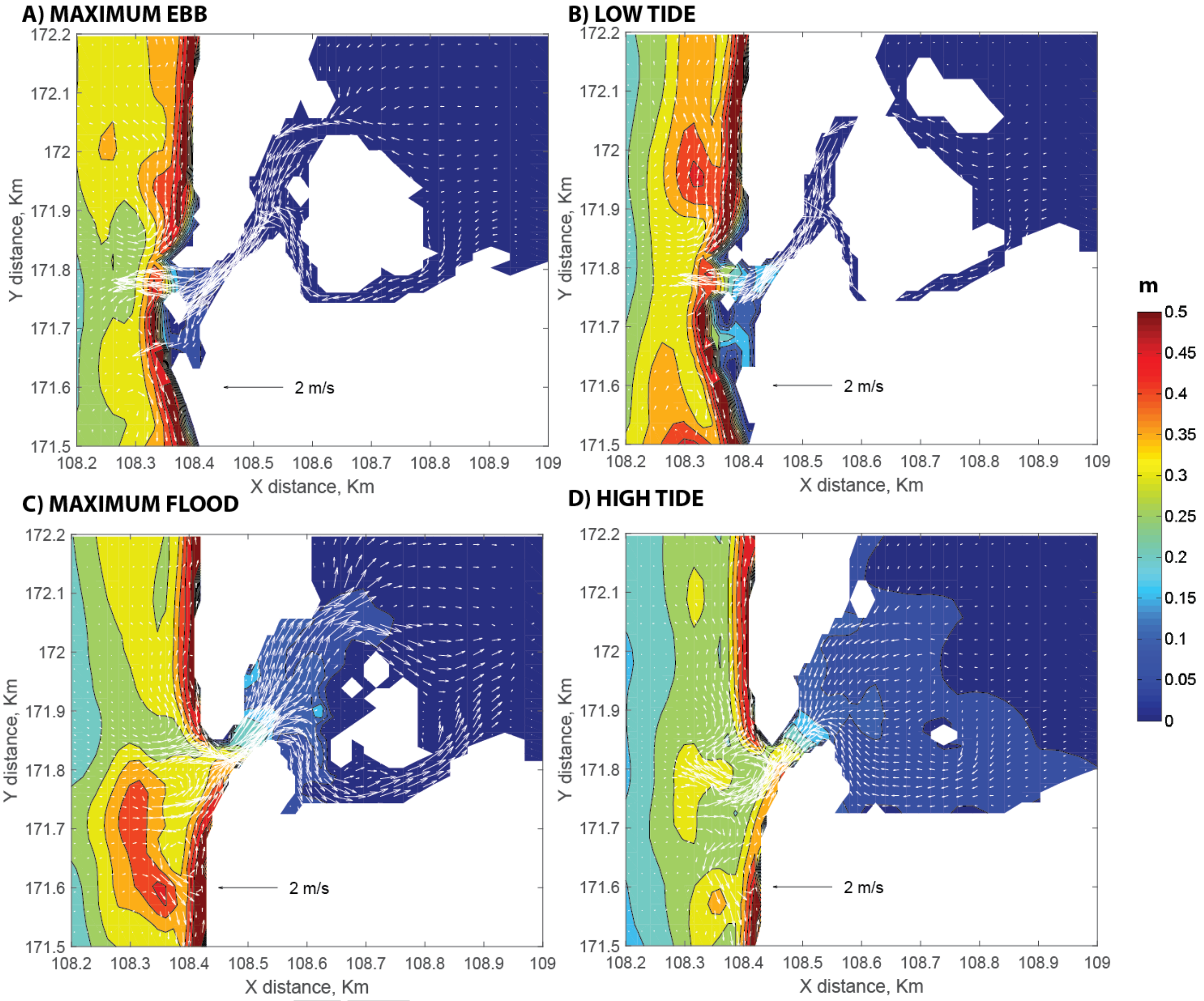

Figure9. Simulated $H_{m0,IG}$ distribution and depth-averaged current vectors during a) maximum ebb, b) low-tide, c) maximum flood, and d) high-tide of the last tidal cycle. Current vectors were averaged over the length of the burst (30 minutes). High tide and low tide are defined in terms of maximum and minimum water levels inside the lagoon.

Gravity waves at inlets get blocked during the maximum ebb and they break at or before the blocking point without being reflected, while losing considerable amounts of energy due to current induced whitecapping (Chawla and Kirby, 2002). Similarly, IG waves could be blocked at the inlet and this could explain the drastic energy damping observed during the mid-ebb and low tide between PT1 and the inner stations, both in the measurements and in the model. Wave blocking happens when the absolute wave group celerity falls to zero, in other words, when the relative group celerity is equal to the opposing current speed:

$$C_{g,a} = C_{g,r} + U\cos\alpha = 0 \quad (6)$$

where $C_{g,a}$ and $C_{g,r}$ are the absolute and relative wave group celerities, respectively, U is the vertically averaged current speed and α is the angle between waves and currents. When blocking occurs, the wave energy cannot propagate against the current.

The linear wave dispersion relationship affected by the Doppler shift can be used to determine the maximum period blocked by an opposing current with a given intensity:

$$\sigma^2 = \left(w_a - kU\cos\alpha\right)^2 = gk\tanh(kh) \quad (7)$$

Where σ is the intrinsic or relative frequency, w_a is the absolute frequency, U the magnitude of the depth-averaged velocity, k is the wavenumber, g the gravitational acceleration and h is the total water depth.

We used the linear dispersion relation to determine, based on the computed water levels and current speeds, where and when gravity and IG wave blocking occurred. As shown in Figure 10 (panels a and b), weaker opposing current speeds are required to block shorter period waves according to the linear dispersion relation. For 1 m water depth, current velocities larger than 2.4 m.s^{-1} are theoretically required to block waves of any frequencies while for 0.5 m water depth, this value drops to 1.7 m.s^{-1}. IG wave blocking in the last tidal cycle got initiated at the inlet mouth (Figure 10c), where tidal current speeds up to 2.5 m/s were modeled from mid-ebb to low tide, with water depths varying from 1.5 to 1 m. Gravity-wave blocking was initiated earlier and further offshore.

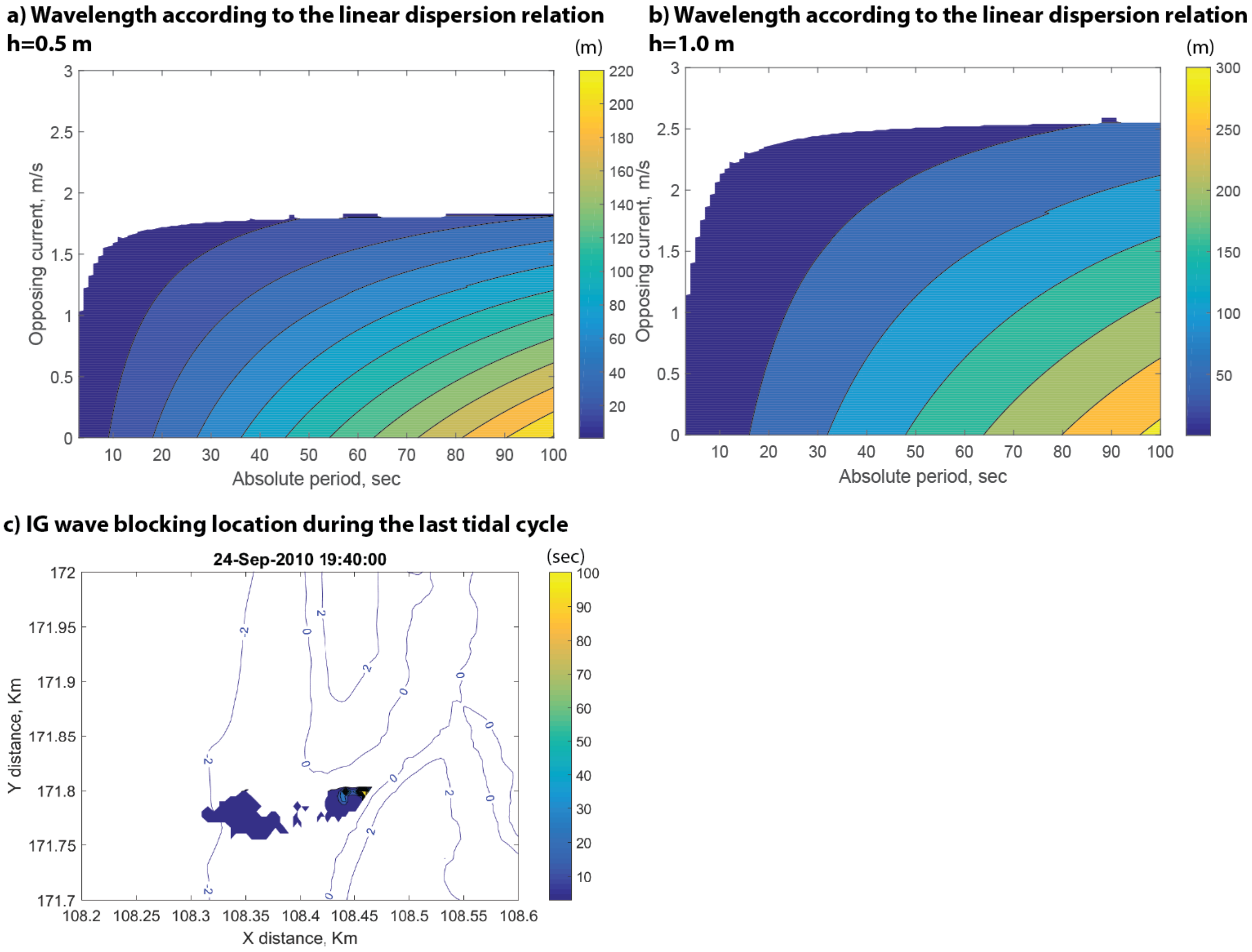

Figure 10. Contour map of the wave length (m) as a function of the opposing current velocity given by the linear dispersion relation, a) for a water depth of 0.5 m and b) for a water depth of 1 m. The white area indicates that there is no real solution and the maximum period indicates the maximum period that is blocked; c) IG wave blocking location computed with the linear-dispersion relation during tidal cycle 3 and bathymetric contour lines in blue. The color indicates the maximum period (s) that is being blocked.

Measured gravity waves at PT2 and PT3 were blocked earlier (20 minutes in average) than the infragravity band (Figures 3, 5 and 6), mainly because lower speed currents and/or larger water depth are required to block lower period waves (Figure 10).

5.4 Possible impacts on sediment dynamics

The propagation of IG waves across the inlet induced current fluctuations that reached more than 50% of the tidal current intensity at PT2 during all the experiment, but especially in the third tidal cycle (Figure 4). Although this behavior was reasonably reproduced by XBeach, a direct comparison with the measured time series was not possible because the phase of the gravity wave frequency components at the offshore boundary were unknown. Alternatively, the standard deviation of current velocities were computed over 30 minute samples and compared. This comparison revealed that XBeach was able to capture the temporal pattern of these low-frequency fluctuations, although with a substantial underestimation of the peak, which occurred during the maximum flood currents. Because sand fluxes depend non-linearly both on water levels and currents, they may be affected by the presence of low-frequency fluctuations associated with IG waves.

These low frequency fluctuations associated with IG waves would tend to promote sand fluxes, but their blocking during a large part of the ebb would cause this process to be more active during the flood. Over a tidal cycle, this process would tend to limit ebb-dominance in the main channel and promote flood-dominance inside the lagoon. One should keep in mind that this experiment was carried out under low to moderate energy waves and it can be expected that under storm waves, larger IG waves would induce larger current fluctuations which could have a determinant impact on the inlet sediment dynamics. In particular, this mechanism could potentially contribute to the shoaling and closure of tidal inlets that occurs in winter along the western coast of Portugal (Bertin et al., 2009; Dodet et al., 2013; Fortunato et al., 2014). Further field measurements should be carried out under storms and under less energetic but more frequent swell conditions, with a deployment specifically dedicated at measuring IG waves and their subsequent dynamics.

6. SUMMARY AND CONCLUSIONS

Field measurements conducted at the Albufeira Lagoon Inlet revealed that IG waves developed on the ebb-tidal delta and propagated inside the lagoon during flood and high tide, while they were blocked during the ebb. The field experiment covered three tidal cycles, during spring tides. Offshore significant wave height and the peak period increased due to the effect of a remote storm that generated energetic swell conditions that impacted the study zone at the end of the experiment. During the last tidal cycle, when the offshore waves were most energetic, $H_{mo,IG}$ values over 0.5 m were measured at the ebb-tidal delta. Inside the lagoon values up to 0.2 m were measured.

The comparison between measurements and numerical simulations showed that IG wave generation and propagation were fairly reproduced with XBeach. This fact indicates that, although XBeach simplifies and neglects some physical processes that can affect both the generation and the propagation of IG waves, the model captures the main processes. The analysis of model results revealed that the two proposed IG wave generation mechanisms (the breaking point variation or dynamic set-up and shoaling and release of the bound-wave) were relevant, and contributed significantly to the IG wave generation. While the bound-wave shoaling was dominant offshore the breaking area, wave breaking contribution was slightly higher from the ebb-tidal delta to the inlet mouth. Model results also suggest that interactions between bound-wave shoaling and the dynamic set-up, produced a reduction of IG energy levels within the surf-zone.

IG waves were shown to be blocked during the ebb, due to strong counter tidal currents in shallow water depths. IG wave blocking occurred later than the gravity-band blocking because stronger opposing currents and shallower depths are needed to block longer period waves.

Field measurements and XBeach simulations demonstrated that, at least at this specific inlet, IG wave generation, propagation, and dissipation mechanisms differed substantially from those observed in beach environments. Due to steep bottom slopes at the terminal- lobe and gentle slopes in the inner part of the ebb-tidal delta, the bound-wave shoaling and release and the "dynamic" set-up mechanisms were both active during the analyzed period. Moreover, results have shown another relevant difference with respect to the beach environments: while in beach environments the IG wave energy is dissipated or reflected in the coast, in tidal inlets the energy is partially transmitted to the inner part of the lagoon depending on the water levels and tidal currents at the inlet.

Both measurements and model results showed that IG waves induced fluctuations in flood currents inside the lagoon reaching temporarily 100 % of the low-pass filtered current magnitudes (although the largest fluctuations were underestimated in the model). The fact that these fluctuations occur mostly at flood and not at ebb because IG waves are blocked could promote flood dominance in the lagoon. This mechanism could contribute the shoaling and closure of tidal inlets, in combination to other wave-induced processes previously analyzed (e.g. Bertin et al., 2009; Dodet et al., 2013). However, the field experiment presented in this study was carried out under low to moderate wave energy and doesn't allow for a quantification of the impact of IG waves on the inlet sediment dynamics. Additional field measurements designed to measure infragravity wave propagation and transformation, the implications on the fluctuation of currents and the subsequent impacts on sediment transport dynamics will have to be carried out in such shallow inlets, under storm waves and mean wave conditions.

ACKNOWLEDGEMENTS

These results were acquired in the scope of the research projects MOWADI funded by the Portuguese Foundation for Science and Technology and DYNAMO founded by the French national agency for research (grant agreement n°ANR-12-JS02-00008-01). The colleagues from LNEC and Lisbon University are greatly acknowledged for their help on the field. Guillaume Dodet is thanked for his preliminary processing of the data in the scope of his PhD. The second author benefited from a visiting research grant in La Rochelle University from Region Poitou-Charente. Finally, the developing team of X-Beach is sincerely acknowledged. The numerical results and some of the processed data used in this paper will be made available upon request to the authors. The suggestions of three anonymous reviewers were greatly appreciated and improved this manuscript substantially.

APPENDIX A

Considering that $M_n$and $C_n$are the measured data and thecomputed data, respectively, at N discrete points, the model performance (skill, S) formula proposed by Wilmott (1981) is given by:

$$S = 1 - \frac{\frac{1}{N}\sum_{n=1}^{N}\left|C_n - M_n\right|^2}{\sum_{n=1}^{N}\left(\left|C_n - \overline{M}_n\right| + \left|M_n - \overline{M}_n\right|\right)^2}$$

The overbar represents the mean value.This skill factor ranges from 0 (bad skill) to 1 (very good skill).

REFERENCES

Arnaud, G., et X. Bertin (2014), Contribution du setup induit par les vagues dans la surcote associée à la tempête klaus. XIII èmes Journées Nationales Génie Côtier _ Génie Civil, pp. 859_867.

Baldock, T. E. (2012), Dissipation of incident forced long waves in the surf zone—Implications for the concept of "bound" wave release at short wave breaking, *Coastal Eng.*, 60, 276–285, doi:10.1016/j.coastaleng.2011.11.002.

Baldock, T.E., O'Hare, T.J., Huntley, D.A., (2004), Long wave forcing on a barred beach,*J. Fluid Mech.* 503, 321–343.

Baldock, T. E., and D. A. Huntley (2002), Long-wave forcing by the breaking of random gravity waves on a beach, Proc. R. Soc. London, Ser. A, 458, 2177–2201.

Battjes, J. A., H. J. Bakkenes, T. T. Janssen, and A. R. van Dongeren (2004), Shoaling of subharmonic gravity waves, J. Geophys. Res., 109, C02009, doi:10.1029/2003JC001863.

Bendat, J.S. and Piersol, A.G., 1971. Random Data: Analysis and Measurement Procedures. John Wiley and Sons, New York, NY.

Bertin, X., A. B. Fortunato, and A. Oliveira, A., (2009), A modelling-based analysis of processes driving wave-dominated inlets, *Cont. Shelf Res.*, 29, 819–834.

Bertin, X., Li, K., Roland, A., Bidlot, J.-R., (2015), The contribution of short-waves in storm surges: two case studies in the Bay of Biscay,*Cont. Shelf Res.* 96, 1-15.

Bonneton, E. Barthelemy, F. Chazel, R. Cienfuegos, D. Lannes, F. Marche, M. Tissier, (2011),Recent advances in Serre–Green Naghdi modelling for wave transformation, breaking and runup processes,*Eur. J. Mech. B, Fluids*, 30, pp. 589–597

Booij, N., Ris, R.C. & Holthuijsen, L.H., (1999), A third-generation wave model for coastal regions, Part I, Model description and validation, *J.Geoph.Research*, 104, C4, 7649-7666.

Chawla, A. and Kirby, J.T. (2002), Monochromatic and random wave breaking at blocking points,*J. of Geophys. Res.* 107: doi: 10.1029/2001JC001042.

Chen, J.-L., T.-J. Hsu, F. Shi, B. Raubenheimer, and S. Elgar, 2015. Hydrodynamic and sediment transport modeling of New River Inlet (NC) under the interaction of tides and waves, *J. Geophys. Res.* Oceans, 120, doi:10.1002/2014JC010425.

Crawford, W., Ballu, V., Bertin, X. and Karpytchev, M., (2015), The sources from deep-ocean infragravity waves in the North Atlantic Ocean, J. Geophys. Res. Oceans, 120, 5120–5133, doi:10.1002/2014JC010657.

Daly, C., D. Roelvink, A. van Dongeren, J. van Thiel de Vries, R. McCall, (2012). Validation of an advective-deterministic approach to short wave breaking in a surf-beat model, Coastal

Engineering, Vol 60, February 2012, 69-83, ISSN 0378-3839.

Dee D. P., S. M. Uppala, A. J. Simmons *et al.*(2011), The ERA-Interim reanalysis: configuration and performance of the data assimilation system, *Q.J.R. Meteorol. Soc.*, 137(656), 553-597, doi:10.1002/qj.v137.656.

Dodet, G., (2013), Morphodynamic modelling of a wave-dominated tidal inlet: the Albufeira Lagoon, unpublished PhD Thesis, La Rochelle University, France, 207pp.

Dodet, G., Bertin, X., and Taborda, R., (2010), Wave climate variability in the North-East Atlantic Ocean over the last six decades,*Ocean Modelling*, 31: 120-131.

Dodet, G., X. Bertin, N. Bruneau, A. B. Fortunato, A. Nahon, and A. Roland, (2013), Wave-current interactions in a wave-dominated tidal inlet, *J. Geophys. Res. Oceans*, 118, 1587–1605, doi: 10.1002/jgrc.20146.

Eldeberky, Y., (2015),Applicability of a Stochastic Model to Nonlinear Shoaling of Surface Waves,*Coast. Eng. J.*, 57, 1550002 DOI: 10.1142/S0578563415500023.

Fortunato, A.B., Nahon, A., Dodet, G., Rita Pires, A., Conceição Freitas, M., Bruneau, N., Azevedo, A., Bertin, X., Benevides, P., Andrade, C. and Oliveira, A. (2014),Morphological evolution of an ephemeral tidal inlet from opening to closure: The Albufeira inlet, Portugal,*Cont. Shelf Res.* 73, 49-63.

Galappatti, R., and C. B. Vreugdenhil, (1985) A depth-integrated model for suspended sediment transport, *J. Hydraul. Res.*, 23(4), 359– 377,.

Grant, W.D., Madsen, O.S., (1979), Combined wave and current interaction with a rough bottom,*J. of Geophys. Res.* 84 (C4), 1797–1808.

Guza, R. T., E. B. Thornton, and R. A. Holman (1984), Swash on steep and shallow beaches, in Proceedings of the Coastal Engineering Conference, 1984, edited by B. L. Edge, pp. 708–723, Am. *Soc. of Civ. Eng.*, Reston, Va.

Hasselmann, K., (1962), On the non-linear transfer in a gravity spectrum, Part 1. General theory,*J. Fluid Mech.*, 12, 481-500.

Herbers, T.H.C., Elgar, S., Guza, R.T, (1994), Infragravity-frequency (0.005–0.05 Hz)motions on the shelf, part I, Forced waves,*J. Phys. Oceanogr.* 24, 917–927.

Herbers, T.H.C., Elgar, S., Guza, R.T, (1995), Generation and propagation of infragravitywaves,*J. Geophys. Res.* 100, 24, 863–24, 872.

Kennedy, A., Chen, Q., Kirby, J., and Dalrymple, R. (2000),Boussinesq Modeling of Wave Transformation, Breaking, and Runup.I: 1D,*J. Waterway, Port, Coastal, Ocean Eng.*, 126(1), 39–47.

List, J. H. (1992), A model for the generation of two-dimensional surfbeat, *J. Geophys. Res.*, 97, 5623– 5635.

Long, J. W., and H. T. Özkan-Haller (2009), Low-frequency characteristics of wave group–forced vortices, *J. Geophys. Res.*, 114, C08004,doi:10.1029/2008JC004894.

Longuet-Higgins, M. S., and R. W. Stewart (1962), Radiation stress and mass transport in gravity waves, with application to 'surf beats', *J. Fluid Mech.*, 13, 481–504.

Longuet-Higgins, M. S., and R. W. Stewart (1964), Radiation stresses in water waves: A physical discussion, with applications, *Deep Sea Res.*, 11, 529–562.

Ma, G., F. Shi, J.T. Kirby (2012). Shock-capturing non-hydrostatic model for fully dispersive surface wave processes, Ocean Modelling, Volumes 43-44, 2012, Pages 22-35.

Madsen, P. A., Sørensen, O. R., and Schäffer, H. A. (1997), Surf zone dynamics simulated by a Boussinesq-type model. Part II: Surf beat andswash oscillations for wave groups and irregular waves,*Coast. Eng*., 32, 289–319.

Malhadas, M. S., Leitao, P. C., Silva, A., and Neves, R. (2009), Effect of coastal waves on sea level in Óbidos Lagoon, Portugal, *Cont. Shelf Res.*, 19 9 , 1240–1250.

Masselink, G. (1995), Group bound long waves as a source of infragravity energy in the surf zone, *Cont. Shelf Res.*, 15, 1525–1547.

Okihiro, M., Guza, R. T., (1996),Observations of Seiche Forcing and Amplification in Three Small Harbours,*J. Waterw. Port Coast. Ocean Eng.* 122(5),232–238.

Olabarrieta, M., J. C. Warner, and N. Kumar, (2011), Wave-current interaction in Willapa Bay, *J. Geophys. Res.*, 116, C12014, doi:10.1029/ 2011JC007387.

Olabarrieta, M., W. R. Geyer, and N. Kumar, (2014), The role of morphology and wave-current interaction at tidal inlets: An idealized modeling analysis, *J. Geophys. Res. Oceans*, 119, 8818–8837, doi:10.1002/2014JC010191.

Orescanin, M., B. Raubenheimer, and S. Elgar, (2014), Observations of wave effects on inlet circulation, *Cont. Shelf Res.*, 82, 37–42.

Pomeroy, A., R. Lowe, G. Symonds, A. Van Dongeren, and C. Moore (2012), The dynamics of infragravity wave transformation over a fringing reef, *J. Geophys. Res.*, 117, C11022, doi:10.1029/2012JC008310.

Reniers, A.J.H.M., Groenewegen, M.J., Ewans, K.C., Masterton, S., Stelling, G.S., Meek, J., (2010), Estimation of infragravity waves at intermediate water depth,*Coastal Eng.* 57, 52–61.

Reniers, A.J.H.M., MacMahan, J., Thornton, E.B., Stanton, T.P., (2006), Modelling infragravity motions on a rip-channel beach,*Coast. Eng.* 53, 209–222.

Reniers, A.J.H.M., Thornton, E.B., Stanton, T.P., Roelvink, J.A., (2004), Vertical flow structure during Sandy Duck: observations and modeling,*Coast. Eng.* 51, 237–260.

Rijnsdorp, D. P., G. Ruessink, and M. Zijlema (2015), Infragravity-wave dynamics in a barred coastal region, a numerical study, J. Geophys. Res. Oceans, 120, 4068-4089, doi:10.1002/2014JC010450

Roelvink J.A., Reniers A.J.H.M., Van Dongeren A.R., Van Thiel de Vries J.S.M., McCall R.T., Lescinski J., (2009), Modeling storm impacts on beaches, dunes and barrier islands, *Coast. Eng.*, 56 (11-12), 1133-1152, doi: DOI: 10.1016/j.coastaleng.2009.08.006.

Ruju, A., Lara, J., Losada, I., 2012. Radiation stress and low-frequency energy balance within the surf zone: A numerical approach, Coastal Engineering 68, 44-55.

Schäffer H.A, (1993), Infragravity waves induced by short wave groups,*J. Fluid Mech.* 247, 551–588.

Sénéchal, N., P. Bonneton, and H. Dupuis (2001), Field observations of irregular wave transformation in the surf zone, in *Coastal Dynamics* ’01,pp. 62– 71, Am. Soc. of Civ. Eng., Reston, Va.

Sheremet, A., J.R. Davis,M.Tian,J.L.Hanson,K.K.Hathaway, 2016.TRIADS:A phase-resolving model for nonlinear shoaling of directional wave spectra. Ocean Modelling 99, 60–74.

Siegle, E., D. A. Huntley, and M. A. Davidson, (2004), Physical controls on the dynamics of inlet sandbar systems, *Ocean Dyn.*, 54(3–4), 360–373.

Soulsby, R. (1997), Dynamics of marine sands, a manual for practical applications,. Thomas Telford, ISBN 0-7277-2584X, H.R. Wallingford, England, 249 pp.

Symonds, G., Huntley, D.A, Bowen, A.J, (1982), Two-dimensional surf beat: long wave generation by a time-varying breakpoint,*J. Geophys. Res.* 87, 492–498.

Tolman H. L. (2009), User manual and system documentation of WAVEWATCH III TM version 3.14, Technical note, MMAB Contribution, 276, 220.

Torres-Freyermuth, A., J.L. Lara, I.J. Losada, (2010), Numerical modelling of short-and long-wave transformation on a barred beach, *Coast. Eng.*, 57 (2010), pp. 317–330.

Uchiyama, Y., and J. C. McWilliams (2008), Infragravity waves in the deep ocean: Generation, propagation, and seismichum excitation, *J. Geophys. Res.*, 113, C07029, doi:10.1029/2007JC004562.

van Dongeren, A., J. Battjes, T. Janssen, J. van Noorloos, K. Steenhauer, G. Steenbergen, and A. Reniers (2007), Shoalingand shoreline dissipation of low-frequency waves, *J. Geophys. Res.*, 112, C02011, doi:10.1029/2006JC003701.

Wargula, A., B. Raubenheimer, and S. Elgar (2014), Wave-driven along-channel subtidal flows in a well-mixed ocean inlet, *J. Geophys. Res.* Oceans, 119, 2987–3001, doi:10.1002/2014JC009839.

Willmott, C. J. (1981), On validation of models, Phys. Geogr., 2, 184– 194.

Zijlema, M., Stelling, G. and Smit, P., (2011), SWASH: An operational public domain code for simulating wave fields and rapidly varied flows in coastal waters, *Coast. Engng.*, 58, 992-1012.